


Photogalvanic effects in symmetry broken nodal ring materials

J. W. Zuber and Chao Zhang 

School of Physics and Institute for Superconducting and Electronic Materials, University of Wollongong, New South Wales 2522, Australia



(Received 14 January 2021; accepted 14 May 2021; published 27 May 2021)

Nodal ring semimetals are a class of topological material characterized by a one-dimensional circular region of band crossing in momentum space. The presence of spin-orbit coupling, whether extrinsic or intrinsic, may change the parent nodal ring phase to a Weyl semimetal, Dirac semimetal, or topological insulator child phase. We investigate second harmonic generation and circular photogalvanic effect in the mid-infrared region of nodal ring materials where spin-orbit coupling produces a Weyl semimetal child phase (such as in ZrTe_5 and CaP_3). Spin-orbit coupling breaks the symmetries protecting the nodal ring, inducing a nontrivial Berry curvature which gives rise to colossal photocurrents up to the order of $10^3 \mu\text{A}/\text{V}^2$ at the interband harmonic. Our results are found to be rather robust to parameters such as Fermi level, residual scattering rate, and the number of Weyl points. However, decreasing temperature tends to destroy the harmonic peaks and changing the nodal ring radius drastically alters the harmonic condition, shifting the peak frequency. Equivalent calculations and experiments have been carried out for intrinsic Weyl semimetals such as TaAs where the photocurrents calculated and observed were at least one order of magnitude smaller, highlighting that the parent nodal ring phase enhances these optical nonlinear phenomena.

DOI: [10.1103/PhysRevB.103.205307](https://doi.org/10.1103/PhysRevB.103.205307)

I. INTRODUCTION

Owing to their intriguing and experimentally desirable transport properties, topological materials have been the subject of intense research in recent years [1–6]. One of the more recent classes of topological materials is the nodal ring semimetal (NRSM). As opposed to Dirac and Weyl materials which are characterized by singular points in momentum space at which their conduction and valence bands cross, the NRSM is characterized by a one-dimensional ring in momentum space, dubbed the nodal ring (NR), where the conduction and valence bands meet [7–12]. This electronic structure has led to the theoretical exploration and experimental elucidation of many exotic transport properties such as the peaked optical [13–15] and magneto-optical [16–18] conductivities, anisotropic thermionic emission [19], divergent magnetic susceptibility [20], superconductivity [21,22], quantum oscillations [23,24] and anomalies [25], Landau quantization [26,27], and Lifshitz transitions [28]. Candidate NRSM phases have recently been identified in CaAgAs [29], Mg_3Bi_2 [30], and PbTaS [31].

When any noncentrosymmetric material is subject to light irradiation, the resultant photocurrent varies nonlinearly as a function of the electric field(s) of that radiation. The nonlinear terms for other topological materials such as Dirac semimetals (DSMs) and Weyl Semi-Metals (WSMs) have been shown to be appreciable for frequencies as low as the terahertz range [32–35]. For radiation with plane of polarization described by two electric field vectors, the photocurrent induced is of second order in applied electric field and known as photogalvanic current. Depending on the polarization coefficients of the fields, the photocurrent induced can be shift current

(SC) or circularly polarized photogalvanic effect (CPGE) current. Photogalvanic effects in conventional materials underpin many optical devices and solar cells [36–38]. However, for topological materials photogalvanic effects have become a key tool in the diagnosis of topological phase due to their intrinsic relation to Berry phase [39–41]. Taking the WSM as an example, theoretical calculations show a high sensitivity of the CPGE current generated on both the Weyl point (WP) separation and cone tilt parameter in type-II materials [42–48]. This theoretical work has given impetus to recent experimentation with known WSM TaAs, where large SC and CPGE currents have been observed independently [31,49–53].

Due to the inversion, time reversal, and mirror symmetries protecting the NR [54–57], theoretical models describing NRSMs do not exhibit any photogalvanic effects. This had made diagnosing their topological phase difficult in practice. Recent work on the magneto-optical response has revealed giant peaks at frequencies twice the energy of the NR radius [18]. Optically, the weak and smooth rise of the conductivity at frequencies proportional to the NR radius [14,15] makes the NRSM very difficult to diagnose without a magnetic field. Recently, however, emerging classes of NRSMs where spin-orbit coupling (SOC) is intrinsically present or may be extrinsically induced have been studied [8,16,56,58–68]. In this class of material, SOC can break the symmetries protecting the NR, inducing a nonzero Berry curvature and changing the parent NRSM topological phase to either a child WSM (e.g., CrP_2O_7 [69], TlTaSe_2 [70], ZrTe [71]), DSM (e.g., LaN [72], CaTe [73]), or topological insulator (TI) (e.g., CaAgP [74], BaSn_2 [75], CaP_3 [76]) phase. These classes of “symmetry broken NRSMs” are the focus of this paper. Though emerging, some properties have already been theoretically predicted including

optical conductivity, circular dichroism, and radial Hall effects [54,77].

Although photogalvanic effects have been researched at length for intrinsic WSMs there are some conflicting results. For example, Ref. [52] reports a large CPGE with negligible SC, while Ref. [50] reports a large SC, both for TaAs. Furthermore, the limited studies on transport properties of symmetry broken NRSMs show some influence of the parent phase in quantities such as optical conductivity [77]. Hence, photogalvanic effects in symmetry broken NRSMs remains an open problem that should shed light on the diagnosis of emerging materials. Using a second-order Kubo-type formalism we study both the SC and CPGE in a symmetry broken NRSM and the effect of intrinsic and extrinsic parameters such as NR radius and temperature on their frequency dependence. Our studies take place in the mid-infrared (MIR) frequency region, where photon energies are high enough to activate optical transitions [42,50,52]. This is opposed to popular Floquet formalisms compatible with our material [78–80] which deal with higher frequencies.

II. THEORY

A. Electronic and topological properties

In the absence of an external field, the standard Hamiltonian for a NRSM is the 4×4 matrix [7,14,18–20]

$$H^0 = v_F \tau_x \otimes (\boldsymbol{\sigma} \cdot \mathbf{p}) + b \tau_z \otimes \sigma_z, \quad (1)$$

where \mathbf{p} is the momentum vector, $v_F \approx 10^6$ m/s is the Fermi velocity [81], the radius of the nodal ring in the p_x - p_y plane is b/v_F , and $\boldsymbol{\tau}$ and $\boldsymbol{\sigma}$ are the Pauli matrices for two isospin degrees of freedom, i.e., spin sublattices and atomic orbitals. The Hamiltonian in Eq. (1) is readily diagonalized yielding the four-band dispersion

$$E_{s,r}^0 = s \sqrt{(v_F p_z)^2 + (v_F p + r b)^2},$$

where $p = \sqrt{p_x^2 + p_y^2}$, $s, r = \pm 1$ distinguish the four bands. This dispersion is shown graphically in Figs. 1(a) and 1(b). It is readily observed that the NR generated by Eq. (1) is protected by mirror reflection (in the p_z plane), composite (inversion and time-reversal), and chiral symmetries. For our application, where the Fermi level $\mu \ll v_F b$, the wave functions of Eq. (1) can be expanded around the nodal ring and the Hamiltonian projected onto the two-component subspace (single sublattice or orbital) which accounts for the lowest energy bands to obtain a minimal two-band model

$$H^0 = (v_F p - b) \sigma_z + v_F p_z \sigma_y. \quad (2)$$

The wave functions of (2) represent the behavior of carriers close to the NR and capture all necessary information of the system [27,82]. Equation (2) produces identical energy levels to Eq. (1) for the $r = -1$ bands when diagonalized:

$$E_s^0 = s \sqrt{(v_F p_z)^2 + (v_F p - b)^2}. \quad (3)$$

Using Eq. (2), the aforementioned symmetries protecting the NR are given explicitly by (i) mirror reflection symmetry, $\mathcal{M}_z = i \sigma_z : \mathcal{M}_z H_0 \mathcal{M}_z^{-1} = H_0(-p_z)$ [83,84]; (ii) composite inversion ($\mathcal{P} = \sigma_z$) and time-reversal ($\mathcal{T} = \mathcal{K}$) symmetry, $(\mathcal{PK}) H_0 (\mathcal{PK})^{-1} = H_0$ [27,58]; and (iii) chiral symmetry, $\chi =$

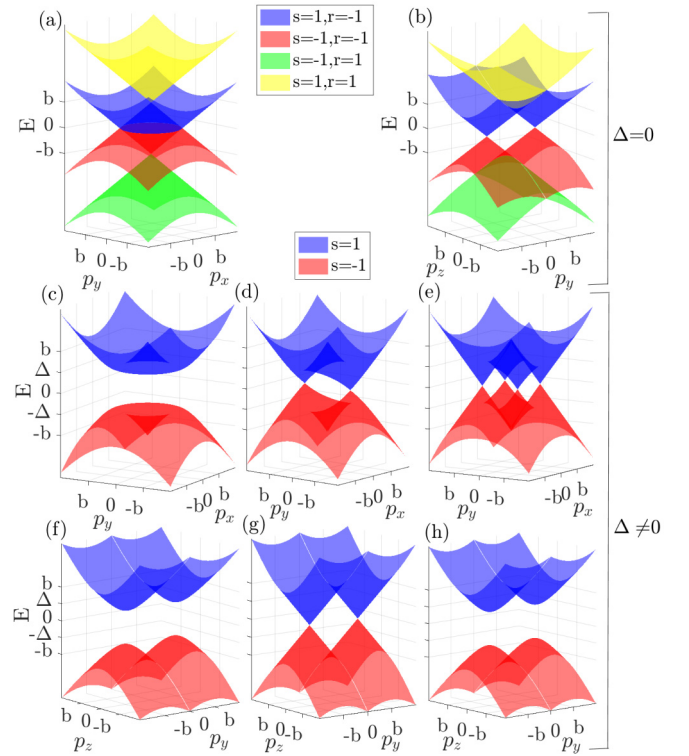


FIG. 1. NRS dispersion relation, without SOC (a) parallel and (b) perpendicular to the ring plane; with SOC parallel to the ring plane with (c) $N = 0$, (d) $N = 1$, and (e) $N = 2$; and with SOC perpendicular to the ring plane with (f) $N = 0$, (g) $N = 1$, and (h) $N = 2$.

$\sigma_x : \chi H_0 \chi^{-1} = -H_0$ [10,85]. In terms of topological properties, the mirror reflection symmetry demands $\sigma_z = \pm 1$ be a good quantum number separating the bands between the NR in the p_z direction. In this way, the NR acts like a band inversion point which is not necessarily destroyed by SOC. Both the composite and chiral symmetries define a $\pm\pi$ quantization of the Berry phase. This Berry phase exists by virtue of one's ability to assign a winding number to any one-dimensional (1D) manifold enclosing an energy gap [10,84]. Although SOC always breaks the composite symmetry, it may be compatible with chiral symmetry [77].

If the NR remains protected by the three symmetries described above, the material will exhibit no photogalvanic effects. This is a direct result of the triviality of the Berry curvature, which is defined in momentum space as

$$\begin{aligned} \boldsymbol{\Omega}_s &= -\text{Im}(\langle \nabla_{\mathbf{p}} \psi_s | \times | \nabla_{\mathbf{p}} \psi_s \rangle) \\ &= -\text{Im}(\langle \partial_{p_y} \psi_s | \partial_{p_z} \psi_s \rangle - \langle \partial_{p_z} \psi_s | \partial_{p_y} \psi_s \rangle) \hat{x} \\ &\quad + \text{Im}(\langle \partial_{p_x} \psi_s | \partial_{p_z} \psi_s \rangle - \langle \partial_{p_z} \psi_s | \partial_{p_x} \psi_s \rangle) \hat{y} \\ &\quad - \text{Im}(\langle \partial_{p_x} \psi_s | \partial_{p_y} \psi_s \rangle - \langle \partial_{p_y} \psi_s | \partial_{p_x} \psi_s \rangle) \hat{z}, \end{aligned} \quad (4)$$

where $s = \pm 1$ for each band and ψ_s are the Bloch wave functions obtained from the time-independent Schrödinger equation. The composite symmetry forces $\boldsymbol{\Omega}_s = 0$ as a result of \mathcal{T} -symmetry demanding $\boldsymbol{\Omega}_s(\mathbf{p}) = -\boldsymbol{\Omega}_s(-\mathbf{p})$ while \mathcal{P} -symmetry demands $\boldsymbol{\Omega}_s(\mathbf{p}) = \boldsymbol{\Omega}_s(-\mathbf{p})$. Similarly, chiral symmetry forces $\boldsymbol{\Omega}_{+1} = \boldsymbol{\Omega}_{-1} = 0$ with the last equality

coming from the fact that the total Berry curvature must vanish [84].

To induce a nonzero Berry curvature (and nonzero photogalvanic effect) we introduce the term $\Delta \cos(N\phi)\sigma_x$ into Eq. (2) producing the system Hamiltonian [77]

$$H = \begin{pmatrix} v_F p - b & -iv_F p_z + \Delta \cos(N\phi) \\ iv_F p_z + \Delta \cos(N\phi) & -(v_F p - b) \end{pmatrix}, \quad (5)$$

where Δ describes the strength of SOC, $N \in \mathbb{Z}$, and ϕ is the azimuthal angle (in the plane of the nodal ring). Diagonalizing Eq. (5) produces the following dispersion relation:

$$E_s = s\sqrt{(v_F p_z)^2 + (v_F p - b)^2 + \Delta^2 \cos^2(N\phi)}. \quad (6)$$

The dispersion in Eq. (6) is plotted in Figs. 1(c)–1(h). It is readily shown that the $\Delta \cos(N\phi)\sigma_x$ term breaks the chiral,

composite, and mirror reflection symmetries; hence so long as $\Delta \neq 0$ the nodal ring in Eq. (5) is no longer symmetry protected and there may exist a nontrivial Berry curvature.

From Figs. 1(c) and 1(f), the $N = 0$ scenario is seen to produce a topological insulator phase, while for $N > 0$ in Figs. 1(d), 1(e), 1(g), and 1(h) the material is in a type-I WSM phase with N pairs of Weyl points occurring on what was previously the NR where $\cos(N\phi) = 0$. In this way the NRSM may be seen as a parent topological phase for both topological insulators and WSMs.

One main advantage of using a two-band model in Eq. (5) is that the Bloch wave functions can be explicitly obtained and hence the Berry curvature. The two orthonormal Bloch wave functions in the momentum representation are

$$|\psi_s\rangle = \begin{pmatrix} \sqrt{E_s + v_F p - b}/\sqrt{2E_s} \\ (iv_F p_z + \Delta \cos(N\phi))/\sqrt{2E_s(E_s + v_F p - b)} \end{pmatrix},$$

and the Berry curvature components are given by

$$(\boldsymbol{\Omega}_s \cdot \hat{x}) = -\frac{v_F \Delta}{4s p^2 E^3 (sE + v_F p - b)^2} \left[\begin{aligned} & N p_x \sin(N\phi) ((2E^2 - s(v_F p_z)^2)(sE + v_F p - b) - E(v_F p_z)^2) \\ & + v_F p p_y \cos(N\phi) (E^2 + 2E(v_F p - b) + s(v_F p - b)^2) \\ & + 2s p_x N (2sE + v_F p - b) \Delta^2 \cos^2(N\phi) \sin(N\phi) \end{aligned} \right],$$

$$(\boldsymbol{\Omega}_s \cdot \hat{y}) = \frac{v_F \Delta}{4s p^2 E^3 (sE + v_F p - b)^2} \left[\begin{aligned} & N p_y \sin(N\phi) ((2E^2 - s(v_F p_z)^2)(sE + v_F p - b) - E(v_F p_z)^2) \\ & - v_F p p_x \cos(N\phi) (E^2 + 2E(v_F p - b) + s(v_F p - b)^2) \\ & + 2s p_y N (2sE + v_F p - b) \Delta^2 \cos^2(N\phi) \sin(N\phi) \end{aligned} \right],$$

$$(\boldsymbol{\Omega}_s \cdot \hat{z}) = -\frac{v_F \Delta}{4s p E^3 (sE + v_F p - b)^2} v_F p_z \sin(N\phi) (E^2 + s(v_F p - b)(2sE + v_F p - b)),$$

where $E = |E_s|$. It is readily observed that the nonzero Berry curvature is induced solely by the SOC term. Furthermore, $\boldsymbol{\Omega}_{-1} \neq \boldsymbol{\Omega}_{+1}$ as chiral symmetry is violated and most interestingly the Berry curvature is odd in \mathbf{p} if N is even (preserving time-reversal symmetry) and even in \mathbf{p} if N is odd (preserving inversion symmetry). Hence, when considering a centrosymmetric Brillouin zone ($\text{BZ}(\mathbf{k}) = \text{BZ}(-\mathbf{k})$), only odd- N perturbations, where time-reversal symmetry is broken, will give rise to a photogalvanic effect. This is also observed in nonlinear conductivity studies of topological materials [32,33,86,87]. Although composite symmetry is broken for any N , the material remains centrosymmetric under the influence of SOC in that $E(\mathbf{k}) = E(-\mathbf{k})$. In this way, centrosymmetry refers to the even parity of the dispersion under $\mathbf{k} \rightarrow -\mathbf{k}$ without constraining the parity of $\boldsymbol{\Omega}(\mathbf{k})$.

B. Second-order conductivity

We consider the symmetry broken NRSM in Eq. (5) subject to two driving electric fields \mathcal{E}_a and \mathcal{E}_b of frequency ω . The photocurrent

$$J^c = \sigma_{cab} \mathcal{E}_a^* \mathcal{E}_b : \quad a, b, c = x, y, z$$

is calculated by using an effective second-order Kubo formula based on quadratic response theory [88–90] extended to dealing with both linearly and circularly polarized light [42]. Within this model, the second-order conductivity σ_{ab}^c is a third-rank tensor given by

$$\sigma_{cab} = \frac{|e|^3}{(2\pi\hbar)^3 \omega^2} \text{Re} \left\{ e^{i\Phi_{ab}} \sum_{\tilde{\omega}=\pm\omega} \sum_{n,l=\pm 1} \int_{\text{BZ}} d^3\mathbf{p} (N_{F,l} - N_{F,n}) \frac{\langle \psi_n | \hat{v}_a | \psi_l \rangle \langle \psi_l | \hat{v}_b | \psi_l \rangle \langle \psi_l | \hat{v}_c | \psi_n \rangle}{(E_n - E_l - i\hbar\tau^{-1})(E_n - E_l + \hbar\tilde{\omega} - i\hbar\tau^{-1})} \right\}, \quad (7)$$

where BZ represents the first Brillouin zone, $n, l = \pm 1$ distinguish the bands, Φ_{ab} is the phase difference between the two driving fields, $N_{F,l} = \{\exp((E_l - \mu)/k_B T) + 1\}^{-1}$ is the Fermi-Dirac distribution of the charge carriers in the l band,

$\hat{v}_a = \partial_{p_a} H$ is the velocity operator in the momentum representation in the a direction, and τ is the quasiparticle lifetime. It should be stated from the outset that $n \neq l$ as there is no such interband process. After some manipulation of the derivatives,

the matrix units become

$$\begin{aligned}
M_{abc}^{nl} &= \langle \psi_n | \hat{v}_a | \psi_l \rangle \langle \psi_l | \hat{v}_b | \psi_l \rangle \langle \psi_l | \hat{v}_c | \psi_n \rangle \\
&= \langle \psi_n | \partial_{p_a} H | \psi_l \rangle \langle \psi_l | \partial_{p_b} H | \psi_l \rangle \langle \psi_l | \partial_{p_c} H | \psi_n \rangle \\
&= (E_n - E_l) \langle \partial_{p_a} \psi_n | \psi_l \rangle \partial_{p_b} E_l (E_n - E_l) \langle \partial_{p_c} \psi_l | \psi_n \rangle \\
&= (E_n - E_l)^2 \partial_{p_b} E_l \langle \partial_{p_a} \psi_n | \partial_{p_c} \psi_n \rangle. \tag{8}
\end{aligned}$$

If inversion symmetry is broken then time-reversal symmetry (TRS) is respected (even N). The combination of centrosymmetry yielding $E(k) = E(-k)$ and TRS yielding $\sigma(k) = -\sigma(-k)$ makes the integrand in Eq. (7) odd. Under TRS, the matrix units in Eq. (8) satisfy $M_{abc}^{nl}(\mathbf{p}) = -M_{abc}^{nl}(-\mathbf{p})$ and the integrand in Eq. (7) is odd under $\mathbf{p} \rightarrow -\mathbf{p}$. Since we integrate over a centrosymmetric Brillouin zone, $\sigma_{cab} = 0$ if time-reversal symmetry is preserved. Although the preservation of time-reversal symmetry does not necessarily imply the second-order conductivity is zero, this result is consistent with other models and extends to all two-band models where centrosymmetry is also preserved [14,89,90]. One case that should be mentioned is the shift current $\sigma_{iii} : M_{iii}^{nl} = \partial_{p_i} E_l \langle \psi_l | \hat{v}_i | \psi_n \rangle^2 \in \mathbb{R}$ which is obviously odd in \mathbf{p} and yields no response in our model. However, shift current of the form σ_{iii} has been reported as $\approx 4\%$ of the overall photocurrent, not necessarily zero in WSMs [42,52]. Such findings suggest that this type of shift current is not due to a two-band process and one must use a multiband Hamiltonian in order to calculate it. However, as we show, our two-band model proves adequate for calculating all other photogalvanic effects.

Now, in the long relaxation time limit, $\tau \rightarrow \infty \Rightarrow -i\hbar\tau^{-1} \rightarrow 0$, we can use the Sokhotski-Plemelj relations to separate the terms:

$$\begin{aligned}
P^{nl} &= \lim_{\tau \rightarrow \infty} \frac{1}{(E_n - E_l - i\hbar\tau^{-1})(E_n - E_l + \hbar\tilde{\omega} - i\hbar\tau^{-1})} \\
&= i\pi P \left(\frac{\delta(E_n - E_l + \hbar\tilde{\omega})}{E_n - E_l} + \frac{\delta(E_n - E_l)}{E_n - E_l + \hbar\tilde{\omega}} \right) \\
&\quad + \frac{P}{(E_n - E_l)(E_n - E_l + \hbar\tilde{\omega})} \\
&\quad - \pi^2 \delta(E_n - E_l) \delta(E_n - E_l + \hbar\tilde{\omega}), \tag{9}
\end{aligned}$$

where P denotes the principle part of the integral. The long relaxation time limit is a valid approximation for semiconductors and insulators; however, for metallic crystals the function $\delta(E_n - E_l)$ can induce numeric instabilities, especially for driving fields with frequencies below the terahertz region. To combat this we consider frequencies in the MIR range (which is the feature-rich region for typical parameters) and numerically approximate the δ functions by

$$\delta(x) = \frac{1}{\pi} \frac{\gamma\mu}{(\gamma\mu)^2 + x^2},$$

where the parameter $\gamma \approx 10^{-4}$ – 10^{-2} broadens the δ functions to account for a finite residual scattering rate $\gamma\mu$ [86,91,92].

By noting $\Phi_{ab} = 0$ for linear polarized fields and $\Phi_{ab} = \pi/2$ for circularly polarized fields, we determine that the nonzero SC components correspond to taking the imaginary part of Eq. (9) for linearly polarized fields, while the nonzero CPGE components all arise from circularly polarized fields

and taking the real part of Eq. (9). These nonzero components are listed in Table I. By the structure of each part in Eq. (9), we surmise that the SC will exhibit a strong peak whenever the band gap is equal to the photon energy $|E_n - E_l| = \hbar\omega$ as well as the low-frequency Drude peak as $\omega \rightarrow 0$. Although the CPGE current also displays peaks around the same areas in momentum space, the function $\text{Re}(P^{nl})$ is more diffuse, leading to a less peaked response. This trend is also observed when using computational multiband models for intrinsic WSMs [42]. Although we are typically interested in the MIR frequency range for optoelectronic applications, lower-frequency regions can be explored via semiclassical formalism in which $\sigma \propto \int d^3\mathbf{p} \partial_p \Omega$.

Finally, we complete the sums in Eq. (7) analytically using Eq. (4) to directly relate the Berry curvature to both the SC and CPGE conductivities and the remaining azimuthal symmetry to determine the degenerate components in Table I.

III. NUMERICAL RESULTS

Each nondegenerate component of the photoconductivity tensor from Table I is plotted in Fig. 2. The driving laser power is 10 mW. At the charge neutrality point, Fig. 2(b) implies a CPGE photocurrent of 16.512×10^{-4} A parallel to the NR (WP) plane for two perpendicular fields. This value is an order of magnitude larger than other numerical two-band models for the intrinsic WSM TaAs: 1.2×10^{-4} A in Ref. [42] and 1.015×10^{-4} A in Ref. [52]. When including three-band transitions, the CPGE current in Ref. [42] jumps to 29.2×10^{-4} A which agrees well with the experimental result of 4×10^{-4} A in Ref. [52] after considering the scaling factor. Similar magnitude CPGE currents are found in other intrinsic WSMs such as type-II MoTe₂ and Mo_{0.9}W_{0.1}Te₂ [48,51]. It is reasonable to expect a similar increase for the NRSM + SOC if one used a multiband density functional theory (DFT) model to accommodate virtual transitions.

Further, our SC results from Fig. 2(c) imply a photocurrent of 2.112×10^{-4} A along the NR (WP) plane at the charge neutrality point for fields directed perpendicular to the NR (WP) plane. Again our results are slightly larger than the TaAs multiband DFT calculation in Ref. [42] which yields 1.2×10^{-4} A and the experimental results in Ref. [50] which report 0.416×10^{-4} A. Both TaAs values are much larger than the shift current along the z axis of WSM BaTiO₃ experimentally found to be 2×10^{-8} A in Refs. [39,93]. These comparisons show that a two-band effective model is appropriate for calculating second-order nonlinear conductivities of a NRSM + SOC and leads us to postulate that the manifestation of the parent phase in the child dispersion leads to a larger response when compared to intrinsic WSMs by up to an order of magnitude—well within the bounds of variance between WSM compounds.

In terms of frequency characteristics, the diffuse nature of the dispersive part of Eq. (9) is well exhibited in Fig. 2(a). One observes this shift in spectral weight to the lower-frequency region $\hbar\omega \in (0, 0.06)$ eV where the Drude peak decrease meets the interband transition peak at $\hbar\omega \approx 0.75$ eV for $|E_n - E_l| = \hbar\omega$. The harmonic condition is met when the driving field effectively lifts the valence band to a point where the $\mathbf{k} = 0$ saddle points cross; for a two-band model this is precisely

TABLE I. Second-order photoconductivity tensor components. Rows 1–6 represent the SC and rows 7–11 represent the CPGE current.

Tensor component	Degenerate component(s)	$I : \sigma_{cab} = \frac{ e ^3 \pi}{(2\pi\hbar)^3 \omega^2} \int_{BZ} d^3\mathbf{p} (N_{F,1} - N_{F,-1}) E^2 I$
σ_{xxx}		0
σ_{yyy}		0
σ_{zzz}		0
σ_{xzz}	σ_{yzz}	$-\partial_{p_z} E(\mathbf{\Omega}_1 \cdot \hat{y}) \text{Im}(P^{1,-1})$
σ_{zxx}	σ_{zyy}	$\partial_{p_x} E(\mathbf{\Omega}_1 \cdot \hat{y}) \text{Im}(P^{1,-1})$
σ_{xyy}	σ_{yxx}	$\partial_{p_y} E(\mathbf{\Omega}_1 \cdot \hat{z}) \text{Im}(P^{1,-1})$
σ_{xxz}	$\sigma_{yyz}, -\sigma_{xzx}, -\sigma_{yzy}$	0
σ_{yxz}	$\sigma_{xyx}, -\sigma_{yzx}, -\sigma_{xzx}$	$-\partial_{p_z} E(\mathbf{\Omega}_1 \cdot \hat{z}) \text{Re}(P^{1,-1})$
σ_{zxy}	$-\sigma_{zyx}$	$\partial_{p_y} E(\mathbf{\Omega}_1 \cdot \hat{y}) \text{Re}(P^{1,-1})$
σ_{xxy}	$\sigma_{yxy}, -\sigma_{xyx}, -\sigma_{yyx}$	0
σ_{zxx}	$\sigma_{zyz}, -\sigma_{zzy}, -\sigma_{zzx}$	$\partial_{p_z} E(\mathbf{\Omega}_1 \cdot \hat{y}) \text{Re}(P^{1,-1})$

$2E = \hbar\omega$. Comparing Figs. 2(b) and 2(c) it is evident the more diffuse conductivity spectrum of CPGE current detracts from the bandwidth of its peak. For both the SC and CPGE conductivity there exists a secondary higher-order harmonic

peak at $\hbar\omega \approx 0.42$ eV. Furthermore, the CPGE component σ_{zxx} shows a satellite peak at $\hbar\omega \approx 0.12$ eV.

The CPGE components in Fig. 2(b) all exhibit different frequency characteristics. The low-frequency behaviors, and indeed the entire MIR behavior of the minute σ_{yxz} which lacks any harmonic features, agrees with DFT calculations of TaAs [42]. However, both harmonic and oscillatory peaks have been predicted theoretically for WSMs [46,94]. The harmonic peak is shown for fields with plane of polarization perpendicular to the ring plane (σ_{zxx}) while the oscillatory peak is evident for fields with plane of polarization parallel to the ring plane (σ_{zxy}). One feature which has not been reported in any WSM research is the satellite peak for σ_{zxx} , at around 1.5 times the frequency of the first harmonic. We postulate that the σ_{zxx} (σ_{zyz}) satellite peak(s) occurs when the frequency is high enough to stimulate carriers from the zy (zx) plane over the saddle point. This occurs at a higher frequency to the main peak as the plane of polarization is perpendicular to the direction of travel for such carriers. Each peak discussed rapidly decreases with frequency owing to the combination of the ω^{-2} prefactor; physically this is due to the dominance of linear order effects at higher frequencies.

The SC components shown in Fig. 2(c) are less feature rich than their CPGE counterparts. As expected, mostly all the non-Drude contribution to the SC conductivity stems from direct Weyl band transitions around $E_n - E_l = 0.75$ eV and falls sharply thereafter. It is important to note that there is almost a negligible SC along the ring plane when subject to co-planar linear fields (σ_{xyy}).

The high degree of anisotropy of the material is showcased by the large variance in magnitude of curves in Figs. 2(b) and 2(c), reaching up to seven orders of magnitude at the first SC harmonic. As discussed for the CPGE, the existence of directionally dependent features such as harmonic and satellite peaks is another strong indication of anisotropy.

We survey the dependence of the SC conductivity on intrinsic and extrinsic parameters in Fig. 3. Only the SC dependence is shown as the CPGE components obey identical trends. First we note that the conductivity is very robust to Fermi level μ in the MIR region. This was also observed for two-band transitions in TaAs where the CPGE conductivity changed by only $200 \mu\text{A}/\text{V}^2$ at the WP [42]. There exist slightly larger Drude weights for higher Fermi levels as the more energetic carriers require less external stimulation. Perhaps

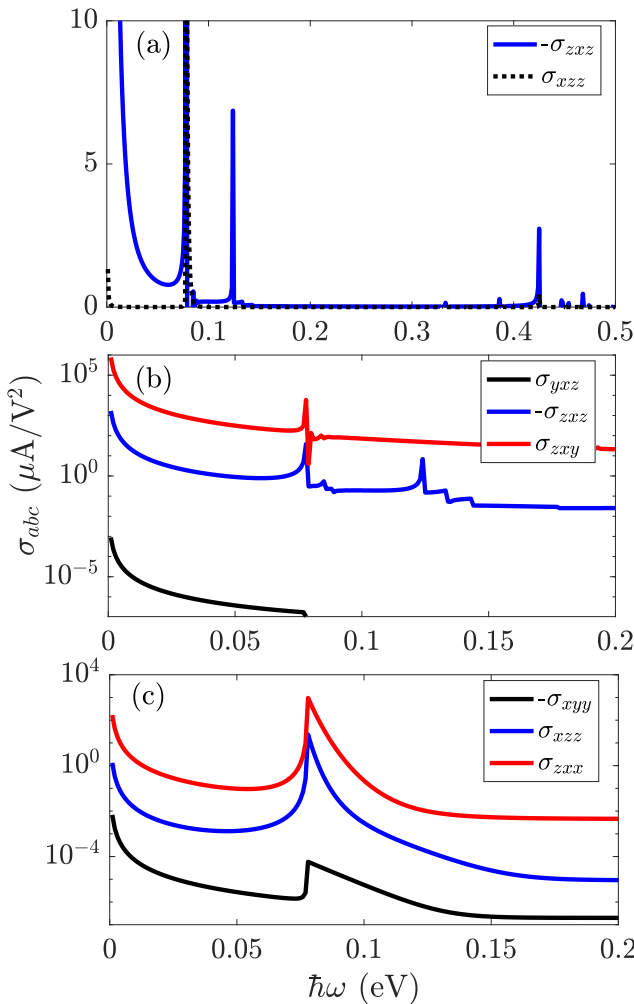


FIG. 2. Nonzero and nondegenerate second-order conductivity tensor components with $v_F = 10^6$ m/s, $\mu = 100$ meV, $\Delta = 33$ meV, $T = 300$ K, $\gamma = 0.001$, $N = 1$, and $b = 8 \times 10^8 v_F \hbar J$.

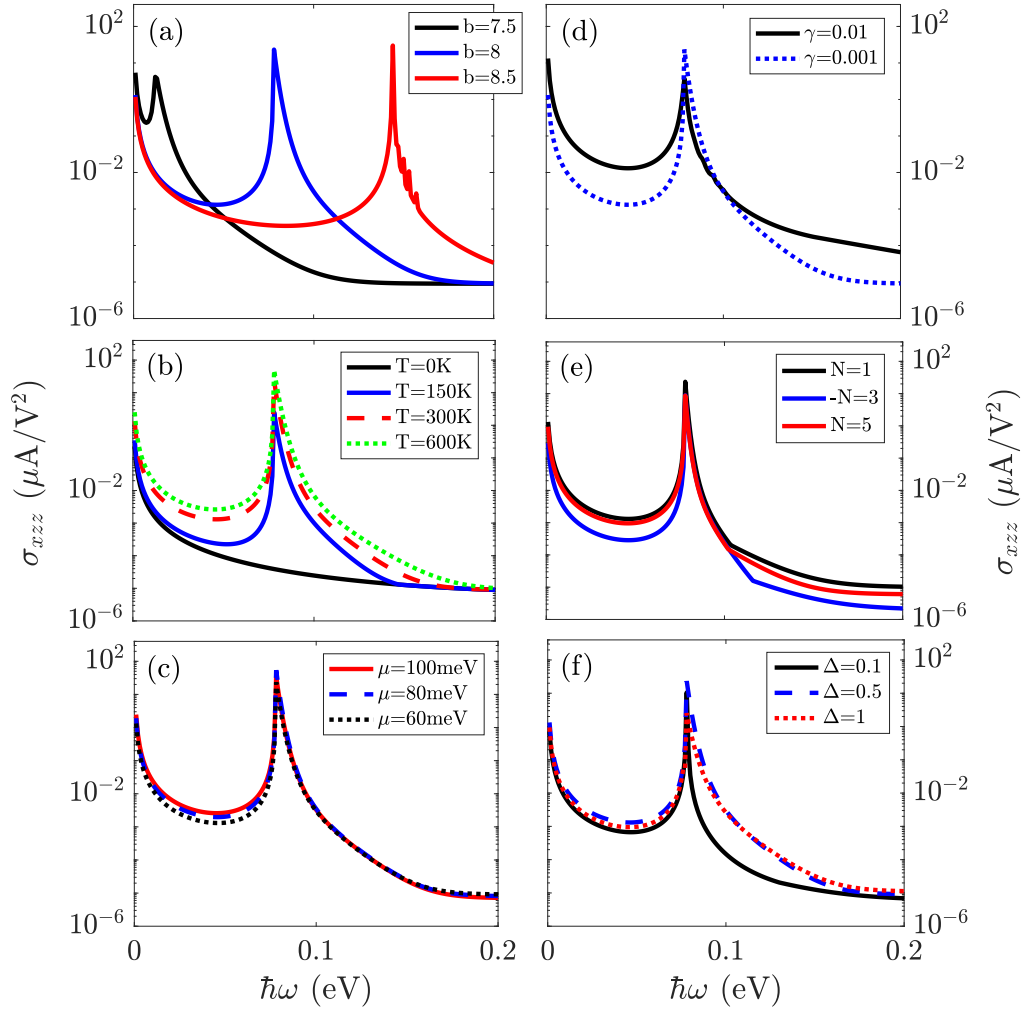


FIG. 3. Parameter dependence of σ_{xzz} . Unless otherwise stated in the legend, the parameters are $v_F = 10^6$ m/s, $\mu = 100$ meV, $T = 300$ K, $\gamma = 0.001$, $N = 1$, $\Delta = 0.5$, and $b = 8$. The units of b are $10^8 v_F \hbar$ J and the units of Δ are 66 meV.

the most straightforward dependencies are on γ and Δ in Figs. 3(d) and 3(f), respectively. The parameter γ controls Drude scattering, which is most prevalent at higher conductivities when the carriers are most mobile. Hence γ narrows all the peak bandwidths as it diminishes. Similarly, higher SOC strengths increase the harmonic bandwidth significantly as the key low-energy carriers experience a larger magnitude Berry curvature. In Fig. 3(e), the number of WPs in the child phase, N , is observed to change the direction of the current for $N = 3$ and slightly diminish the overall response. Although the number of WPs grows (where the bulk of the transitions occur), the spectral width of each WP decreases, as seen in Fig. 1, leading to this smaller conductivity.

The most intriguing parameters are the NR radius b and the temperature shown in Figs. 3(a) and 3(b), respectively. In accordance with the harmonic condition $|E_n - E_l| = \hbar\omega$, increasing b should increase the frequency at which the harmonics occur as the $\mathbf{k} = 0$ saddle point is higher. This is observed in our studies and has also been theoretically predicted for the CPGE peaks in intrinsic WSMs [46]. Unlike WSMs, however, the bandwidth for NRSMs + SOC stays relatively constant when changing b . The peak height also slightly increases with b owing to a greater carrier velocity

near the WPs. The height and bandwidth of the SC conductivity peak is seen to increase appreciably with temperature. Temperature solely enters the numerical scheme via the distribution function $N_{F,l} - N_{F,n} \rightarrow \theta(\mu - E_l) - \theta(\mu - E_n)$ as $T \rightarrow 0$ and since the SC contribution is predominantly from low-energy carriers near the WPs where $E < \mu$, the harmonics are diminished until completely subsiding on the scale of Fig. 3 when $T = 0$.

IV. CONCLUSION

We have analytically determined the Berry phase of a two-band NRSM under the influence of a symmetry breaking SOC term. This SOC term not only induces a nontrivial Berry curvature but produces a WSM child phase. Through quadratic response theory the Berry curvature can be directly related to the second-order CPGE and SC conductivities. Each nondegenerate component of the second-order conductivity tensor was numerically determined in the MIR region in Fig. 2, revealing current responses up to an order of magnitude larger than the equivalent response in intrinsic WSMs [42,48,50–52]. The increased magnitude is attributed to the influence of the parent NR phase.

The conductivity dependence on NR radius (b), temperature, Fermi level, scattering rate, number of pairs of Weyl points, and SOC magnitude are directly observable through our model and showcased in Fig. 3. Although the response is rather robust to many of these parameters, NR radius and temperature both alter the response appreciably. The harmonic peaks almost double in frequency when increasing b just 6.25%, while both the peak height and bandwidth rapidly diminish as temperature falls to zero.

Owing to the high magnitude of our results, we class the symmetry broken NRSMS system as a promising candidate for MIR signal detection and generation. The CPGE response tunability has been used as a diagnosis tool for topological phase in WSMS [48,52]. Given such tunability is shown to persist in the symmetry broken NRSMS we give strong credence to this diagnosis method for concrete materials such as ZrTe₅ [95] or CaP₃ [96] which may be fabricated as single crystals. This tool provides researchers with a method of determining the key topological parameter of NRSMS without the need for a magnetic field [18]. Since both the SOC magnitude and WP separation can be altered by doping [97] or laser fields [98], our results suggest a possibility of engineering a material with desirable frequency response characteristics.

Since our results mostly depend on the dispersion, it is apt to make comment on how real dispersions may deviate from our model. First, the NR is unlikely to resemble a perfect ring in momentum space and in the extremal case resemble a nodal line across the Brillouin zone [16]. The process of linearizing Eq. (1) to Eq. (2) is compatible for nodal line materials and hence we expect the same characteristics to be obtained. The NR may also fluctuate in energy across the Fermi surface. One may deal with this by introducing diagonal terms of the form $D(\mathbf{p})\mathbb{I}_2$ to the Hamiltonian. Since these perturbations will not change the Berry curvature [77] or transition energies, we expect the same qualitative results to be obtained. Finally, since we have concluded most of the optical transitions take place near the nodes, a realistic multiband dispersion consisting of many NRs can be reduced into multiple copies of our model so long as each ring is well separated in momentum space. A more realistic treatment of disorder scattering where τ becomes momentum dependent is also unlikely to change our results since the bulk of transitions occur at low momentum near the nodes.

ACKNOWLEDGMENTS

This research has been supported by the Australian Research Council Grant (Grant No. DP160101474).

-
- [1] K. S. Novoselov, A. K. Geim, S. V. Morozov, D. Jiang, Y. Zhang, S. V. Dubonos, I. V. Grigorieva, and A. A. Firsov, *Science* **306**, 666 (2004).
- [2] K. S. Novoselov, A. K. Geim, S. V. Morozov, D. Jiang, M. I. Katsnelson, I. Grigorieva, S. Dubonos, and A. A. Firsov, *Nature* **438**, 197 (2005).
- [3] M. I. Katsnelson, K. S. Novoselov, and A. K. Geim, *Nat. Phys.* **2**, 620 (2006).
- [4] A. H. Castro Neto, F. Guinea, N. M. R. Peres, K. S. Novoselov, and A. K. Geim, *Rev. Mod. Phys.* **81**, 109 (2009).
- [5] M. Z. Hasan and C. L. Kane, *Rev. Mod. Phys.* **82**, 3045 (2010).
- [6] X. L. Qi and S. C. Zhang, *Rev. Mod. Phys.* **83**, 1057 (2011).
- [7] A. A. Burkov, M. D. Hook, and L. Balents, *Phys. Rev. B* **84**, 235126 (2011).
- [8] L. M. Schoop, M. N. Ali, C. Straßer, A. Topp, A. Varykhalov, D. Marchenko, V. Duppel, S. S. P. Parkin, B. V. Lotsch, and C. R. Ast, *Nat. Commun.* **7**, 11696 (2016).
- [9] N. P. Armitage, E. J. Mele, and A. Vishwanath, *Rev. Mod. Phys.* **90**, 015001 (2018).
- [10] C. K. Chiu, J. C. Y. Teo, A. P. Schnyder, and S. Ryu, *Rev. Mod. Phys.* **88**, 035005 (2016).
- [11] M. Z. Hasan, S. Y. Xu, I. Belopolski, and S. M. Huang, *Annu. Rev. Condens. Matter Phys.* **8**, 289 (2017).
- [12] B. Yan and C. Felser, *Annu. Rev. Condens. Matter Phys.* **8**, 337 (2017).
- [13] S. Barati and S. H. Abedinpour, *Phys. Rev. B* **96**, 155150 (2017).
- [14] J. P. Carbotte, *J. Phys.: Condens. Matter* **29**, 045301 (2017).
- [15] S. P. Mukherjee and J. P. Carbotte, *Phys. Rev. B* **95**, 214203 (2017).
- [16] R. Y. Chen, Z. G. Chen, X.-Y. Song, J. A. Schneeloch, G. D. Gu, F. Wang, and N. L. Wang, *Phys. Rev. Lett.* **115**, 176404 (2015).
- [17] Y. X. Wang, *Eur. Phys. J. B* **90**, 99 (2017).
- [18] W. Duan, C. Yang, Z. Ma, Y. Zhu, and C. Zhang, *Phys. Rev. B* **99**, 045124 (2019).
- [19] S. G. Chen, S. Huang, W. Y. Duan, W. Shi, and C. Zhang, *J. App. Phys.* **128**, 065108 (2020).
- [20] M. Koshino and I. F. Hizbullah, *Phys. Rev. B* **93**, 045201 (2016).
- [21] A. P. Schnyder and S. Ryu, *Phys. Rev. B* **84**, 060504(R) (2011).
- [22] Y. Wang and R. M. Nandkishore, *Phys. Rev. B* **95**, 060506(R) (2017).
- [23] C. Li, C. M. Wang, B. Wan, X. Wan, H.-Z. Lu, and X. C. Xie, *Phys. Rev. Lett.* **120**, 146602 (2018).
- [24] H. Yang, R. Moessner, and L.-K. Lim, *Phys. Rev. B* **97**, 165118 (2018).
- [25] A. A. Burkov, *Phys. Rev. B* **97**, 165104 (2018).
- [26] J. W. Rhim and Y. B. Kim, *Phys. Rev. B* **92**, 045126 (2015).
- [27] K. Mullen, B. Uchoa, and D. T. Glatzhofer, *Phys. Rev. Lett.* **115**, 026403 (2015).
- [28] H. Jiang, L. Li, J. Gong, and S. Chen, *Eur. Phys. J. B* **91**, 75 (2018).
- [29] D. Takane, K. Nakayama, S. Souma, T. Wada, Y. Okamoto, K. Takenaka, Y. Yamakawa, A. Yamakage, T. Mitsuhashi, K. Horiba, H. Kumigashira, T. Takahashi, and T. Sato, *npj Quantum Mater.* **3**, 1 (2018).
- [30] X. Zhang, L. Jin, X. Dai, and G. Liu, *J. Phys. Chem. Lett.* **8**, 4814 (2017).
- [31] J. P. Sun, *Chin. Phys. Lett.* **34**, 077101 (2017).
- [32] J. W. Zuber, T. Zhao, S. Gong, M. Hu, R. B. Zhong, C. Zhang, and S. G. Liu, *Phys. Rev. B* **101**, 085307 (2020).

- [33] S. Shareef, Y. S. Ang, and C. Zhang, *J. Opt. Soc. Am. B* **29**, 274 (2012).
- [34] A. R. Wright, X. G. Xu, J. C. Cao, and C. Zhang, *App. Phys. Lett.* **95**, 072101 (2009).
- [35] S. Huang, M. H. Tran, J. W. Zuber, Q. Wang, Y. Zhu, and C. Zhang, *J. Opt. Soc. Am. B* **36**, 200 (2019).
- [36] I. Grinberg, D. V. West, M. Torres, G. Gou, D. M. Stein, L. Wu, G. Chen, E. M. Gallo, A. R. Akbashev, P. K. Davies, J. E. Spanier, and A. M. Rappe, *Nature* **503**, 509 (2013).
- [37] S. Y. Yang, J. Seidel, S. J. Byrnes, P. Shafer, C. H. Yang, M. D. Rossell, P. Yu, Y. H. Chu, J. F. Scott, J. W. Ager III, L. W. Martin, and R. Ramesh, *Nat. Nanotechnol.* **5**, 143 (2010).
- [38] T. Choi, S. Lee, Y. J. Choi, V. Kiryukhin, and S. W. Cheong, *Science* **324**, 63 (2009).
- [39] S. M. Young and A. M. Rappe, *Phys. Rev. Lett.* **109**, 116601 (2012).
- [40] J. E. Sipe and A. I. Shkrebtii, *Phys. Rev. B* **61**, 5337 (2000).
- [41] T. Morimoto and N. Nagaosa, *Sci. Adv.* **2**, e1501524 (2016).
- [42] Y. Zhang, H. Ishizuka, J. van den Brink, C. Felser, B. Yan, and N. Nagaosa, *Phys. Rev. B* **97**, 241118(R) (2018).
- [43] C.-K. Chan, P. A. Lee, K. S. Burch, J. H. Han, and Y. Ran, *Phys. Rev. Lett.* **116**, 026805 (2016).
- [44] C. K. Chan, N. H. Lindner, G. Refael, and P. A. Lee, *Phys. Rev. B* **95**, 041104(R) (2017).
- [45] L. E. Golub, E. L. Ivchenko, and B. Z. Spivak, *JETP Lett.* **105**, 782 (2017).
- [46] L. E. Golub and E. L. Ivchenko, *Phys. Rev. B* **98**, 075305 (2018).
- [47] D. E. Kharzeev, Y. Kikuchi, R. Meyer, and Y. Tanizaki, *Phys. Rev. B* **98**, 014305 (2018).
- [48] J. Ma, Q. Gu, Y. Liu, J. Lai, P. Yu, X. Zhuo, Z. Liu, J. H. Chen, J. Feng, and D. Sun, *Nat. Mat.* **18**, 476 (2019).
- [49] L. Wu, S. Patankar, T. Morimoto, N. L. Nair, E. Thewalt, A. Little, J. G. Analytis, J. E. Moore, and J. Orenstein, *Nat. Phys.* **13**, 350 (2017).
- [50] G. B. Osterhoudt, L. K. Diebel, X. Yang, J. Stanco, X. Huang, B. Shen, N. Ni, P. Moll, Y. Ran, and K. S. Burch, *Nat. Mat.* **18**, 471 (2019).
- [51] Z. Ji, G. Liu, Z. Addison, W. Liu, P. Yu, H. Gao, Z. Liu, A. M. Rappe, C. L. Kane, E. J. Mele, and R. Agarwal, *Nat. Mat.* **18**, 955 (2019).
- [52] Q. Ma, S.-Y. Xu, C.-K. Chan, C.-L. Zhang, G. Chang, Y. Lin, W. Xie, T. Palacios, H. Lin, S. Jia *et al.*, *Nat. Phys.* **13**, 842 (2017).
- [53] S. Lim, C. R. Rajamathi, V. Süß, C. Felser, and A. Kapitulnik, *Phys. Rev. B* **98**, 121301(R) (2018).
- [54] C. Fang, H. Weng, X. Dai, and Z. Fang, *Chin. Phys. B* **25**, 117106 (2016).
- [55] S. Y. Yang, H. Yang, E. Derunova, S. S. Parkin, B. Yan, and M. N. Ali, *Adv. Phys.: X* **3**, 1414631 (2018).
- [56] Y. Kim, B. J. Wieder, C. L. Kane, and A. M. Rappe, *Phys. Rev. Lett.* **115**, 036806 (2015).
- [57] Y. H. Chan, C.-K. Chiu, M. Y. Chou, and A. P. Schnyder, *Phys. Rev. B* **93**, 205132 (2016).
- [58] H. Weng, Y. Liang, Q. Xu, R. Yu, Z. Fang, X. Dai, and Y. Kawazoe, *Phys. Rev. B* **92**, 045108 (2015).
- [59] R. Yu, H. Weng, Z. Fang, X. Dai, and X. Hu, *Phys. Rev. Lett.* **115**, 036807 (2015).
- [60] H. Weng, C. Fang, Z. Fang, B. A. Bernevig, and X. Dai, *Phys. Rev. X* **5**, 011029 (2015).
- [61] S. M. Huang, S. Y. Xu, I. Belopolski, C. C. Lee, G. Chang, B. Wang, N. Alidoust, G. Bian, M. Neupane, C. Zhang, S. Jia, A. Bansil, H. Lin, and M. Z. Hasan, *Nat. Commun.* **6**, 7373 (2015).
- [62] B. Q. Lv, H. M. Weng, B. B. Fu, X. P. Wang, H. Miao, J. Ma, P. Richard, X. C. Huang, L. X. Zhao, G. F. Chen, Z. Fang, X. Dai, T. Qian, and H. Ding, *Phys. Rev. X* **5**, 031013 (2015).
- [63] S. Y. Xu, I. Belopolski, N. Alidoust, M. Neupane, G. Bian, C. Zhang, R. Sankar, G. Chang, Z. Yuan, C. C. Lee, S. M. Huang, H. Zheng, J. Ma, D. S. Sanchez, B. Wang, A. Bansil, F. Chou, P. P. Shibayev, H. Lin, S. Jia *et al.*, *Science* **349**, 613 (2015).
- [64] M. Offidani and A. Ferreira, *Phys. Rev. B* **98**, 245408 (2018).
- [65] A. David, P. Rakyta, A. Kormányos, and G. Burkard, *Phys. Rev. B* **100**, 085412 (2019).
- [66] M. M. Grujić, M. Z. Tadić, and F. M. Peeters, *Phys. Rev. Lett.* **113**, 046601 (2014).
- [67] T. P. Cysne, A. Ferreira, and T. G. Rappoport, *Phys. Rev. B* **98**, 045407 (2018).
- [68] A. Matos-Abiague and R. L. Rodriguez-Suarez, *Phys. Rev. B* **80**, 094424 (2009).
- [69] B. Zheng, B. Xia, R. Wang, J. Zhao, Z. Chen, Y. Zhao, and H. Xu, *npj Comput. Mater.* **5**, 74 (2019).
- [70] G. Bian, T. R. Chang, H. Zheng, S. Velury, S. Y. Xu, T. Neupert, C. K. Chiu, S. M. Huang, D. S. Sanchez, I. Belopolski, N. Alidoust, P. J. Chen, G. Chang, A. Bansil, H. T. Jeng, H. Lin, and M. Z. Hasan, *Phys. Rev. B* **93**, 121113(R) (2016).
- [71] H. Weng, C. Fang, Z. Fang, and X. Dai, *Phys. Rev. B* **94**, 165201 (2016).
- [72] M. Zeng, C. Fang, G. Chang, Y. A. Chen, T. Hsieh, A. Bansil, H. Lin, and L. Fu, *arXiv:1504.03492*.
- [73] Y. Du, F. Tang, D. Wang, L. Sheng, E. J. Kan, C. G. Duan, S. Y. Savrasov, and X. Wan, *npj Quantum Mater.* **2**, 3 (2017).
- [74] A. Yamakage, Y. Yamakawa, Y. Tanaka, and Y. Okamoto, *J. Phys. Soc. Jpn.* **85**, 013708 (2016).
- [75] H. Huang, J. Liu, D. Vanderbilt, and W. Duan, *Phys. Rev. B* **93**, 201114(R) (2016).
- [76] H. Weng, X. Dai, and Z. Fang, *J. Phys. Condens. Matter* **28**, 303001 (2016).
- [77] Y. Liu, S. A. Yang, and F. Zhang, *Phys. Rev. B* **97**, 035153 (2018).
- [78] Z. Yan and Z. Wang, *Phys. Rev. Lett.* **117**, 087402 (2016).
- [79] A. Narayan, *Phys. Rev. B* **94**, 041409(R) (2016).
- [80] C. K. Chan, Y.-T. Oh, J. H. Han, and P. A. Lee, *Phys. Rev. B* **94**, 121106(R) (2016).
- [81] C. Hwang, D. A. Siegel, S. K. Mo, W. Regan, A. Ismach, Y. Zhang, A. Zettl, and A. Lanzara, *Sci. Rep.* **2**, 590 (2012).
- [82] C. Fang, Y. Chen, H. Y. Kee, and L. Fu, *Phys. Rev. B* **92**, 081201(R) (2015).
- [83] S. A. Yang, H. Pan, and F. Zhang, *Phys. Rev. Lett.* **113**, 046401 (2014).
- [84] F. Zhang, C. L. Kane, and E. J. Mele, *Phys. Rev. Lett.* **111**, 056403 (2013).
- [85] L. S. Xie, L. M. Schoop, E. M. Seibel, Q. D. Gibson, W. Xie, and R. J. Cava, *APL Mater.* **3**, 083602 (2015).
- [86] L. Chen, J. W. Zuber, Z. Ma, and C. Zhang, *Phys. Rev. B* **100**, 035440 (2019).
- [87] Yee Sin Ang, Shareef Sultan, and C. Zhang, *Appl. Phys. Lett.* **97**, 243110 (2010).
- [88] W. Kraut and R. von Baltz, *Phys. Rev. B* **19**, 1548 (1979).
- [89] R. von Baltz and W. Kraut, *Phys. Rev. B* **23**, 5590 (1981).

- [90] N. Kristoffel and A. Gulbis, *Z. Phys. B Condens. Matter* **39**, 143 (1980).
- [91] E. Illes, J. P. Carbotte, and E. J. Nicol, *Phys. Rev. B* **92**, 245410 (2015).
- [92] E. Illes and E. J. Nicol, *Phys. Rev. B* **94**, 125435 (2016).
- [93] A. Zenkevich, Y. Matveyev, K. Maksimova, R. Gaynutdinov, A. Tolstikhina, and V. Fridkin, *Phys. Rev. B* **90**, 161409(R) (2014).
- [94] Z. Li, Y. Q. Jin, T. Tohyama, T. Iitaka, J. X. Zhang, and H. Su, *Phys. Rev. B* **97**, 085201 (2018).
- [95] Q. Li, D. E. Kharzeev, C. Zhang, Y. Huang, I. Pletikosić, A. V. Fedorov, R. D. Zhong, J. A. Schneeloch, G. D. Gu, and T. Valla, *Nat. Phys.* **12**, 550 (2016).
- [96] N. Lu, Z. Zhuo, H. Guo, P. Wu, W. Fa, X. Wu, and X. C. Zeng, *J. Phys. Chem. Lett.* **9**, 1728 (2018).
- [97] A. H. Castro Neto and F. Guinea, *Phys. Rev. Lett.* **103**, 026804 (2009).
- [98] X. J. Liu, M. F. Borunda, X. Liu, and J. Sinova, *Phys. Rev. Lett.* **102**, 046402 (2009).